Contribution to the Laser Welding of wrought and <u>spray-compacted</u> Aluminum Alloys and the Impact of the Alloy Composition on the Welding Microstructure

T. Gietzelt[1)], L. Eichhorn[1)], T. Wunsch[1)], U. Gerhards[1)], T. Przeorski[2)], H. Weiss[2)], R. Dittmeyer [1)]

[1)] Karlsruhe Institute of Technology, Institute for Micro Process Engineering, PO Box 3640, 76021 Karlsruhe, Germany, E-mail: thomas.gietzelt@kit.edu

[2)] PEAK Werkstoff GmbH, Siebeneicker Straße 235, 42553 Velbert

Keywords: laser welding, deep welding, AlMg3, hypereutectic aluminum, pores

<u>Abstract</u>: A wide range of different cw-laser welding parameters in respect to power, focal position and welding velocity were investigated. <u>For AlMg3 the welding velocity was fixed to 3 m/min but different focal positions and powers were applied. Two light-conducting cables with 0.1 and 0.4 mm in diameter leading to different energy densities were used.</u> Several hypereutectic spray-compacted aluminum alloys were welded <u>at 3, 5 and 10 m/min, respectively at two focal positions using the 0.1 mm light-conducting cable</u>. The influence of the welding parameters is discussed in detail. For the conventional alloy AlMg3 containing <u>max. 0.4 % of silicon and 2.6-3.6 % of magnesia</u> shrink pores were observed for a broad range of parameters as reported in the literature. However, there seems to be a narrow window of process parameters to obtain pore free weld seams. For comparison, the spray-compacted hypereutectic aluminum alloys (AlSi17Fe4Cu2.5MgZr, AlSi20Fe5Ni2 and AlSi35Fe2Ni) with silicon contents ranging from 17 to 35 % were investigated in extruded condition. The metallographic microstructure is very different and may support crack free weld seams. <u>The results are compared and emphasize the impact of the energy density on the quality of the weld seams. Since for aluminum even small amounts of alloying elements change the heat conductivity drastically all parameters have to be adjusted carefully.</u>

1. Introduction

In the last decade, by laser welding productivity e. g. in the automotive industry increased extremely. The advantage of the very high velocity of the welding speed reaching several meters per minute allowed the manufacturing of tailored blanks to save weight and material combined with advantageous mechanical properties of this new welding technique compared to spot welding.

Especially for aluminum different papers emphasize the problem of pores. They are attributed to the strong decrease of the solubility of hydrogen when a melt solidifies. The hydrogen is generated from the water bound in the passivation layer. [1, 2] Besides hydrogen, the process of solidification due to the high heat conductivity may play a major role for the formation of shrink pores illustrated later on.

Solidification cracks occur for a wide range of aluminum alloys, depending on the composition. [3] In the literature overviews for different aluminum alloys referring to the chemical composition and its suitability for welding can be found (Figure 1).
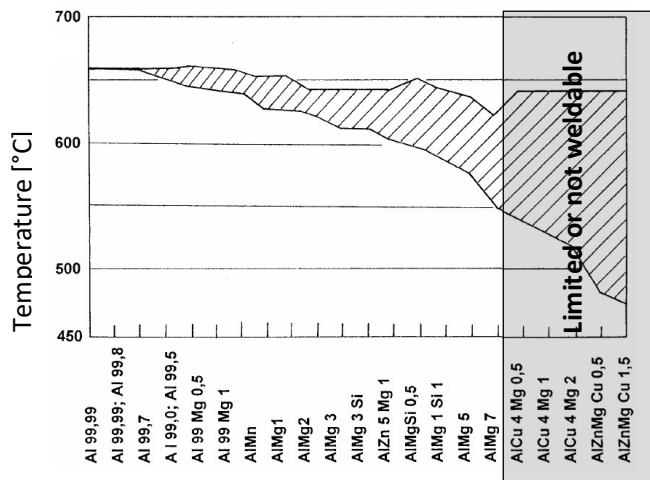
Figure 1: Solidification range and weldability of different aluminum alloys. [4]

The addition of a few percent of other elements widens the solidification temperature range without affecting the high coefficient of thermal expansion. During solidification, the grain growth proceeds according to decreasing temperature. Simultaneously, thermal shrinkage occurs. Finally, thin seams of the remaining melt between the growing grains cause the formation of intercrystalline cracks. Hence, the larger the solidification range of temperature the more an alloy suffers from the sensitivity of hot cracks. Figure 2 shows the influence of the silicon and magnesia content of aluminum on the susceptibility to hot cracks. Preheating of the parts may help to avoid them. However, due to the high thermal conductivity it is not easy to handle and weld the parts at high temperatures. For laser welding, only small parts can be heated inside the welding machine and heat radiation may affect the optical system.

Normally, some pores do not affect the resistance of a weld for construction purposes. However, high vacuum tight weld seams which are necessary for example in process engineering should not contain any pores or cracks.
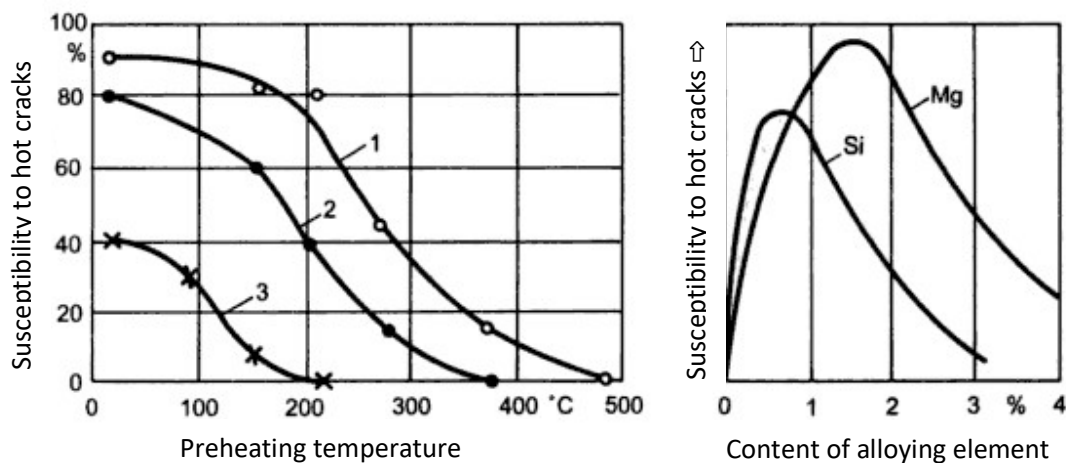

Figure 2: Risk of hot cracks for aluminum alloys depending on preheating temperature and content of the alloying elements Mg and Si. 1: AlMgMn, 2: AlMg2.5; 3: AlMg3.5 according [5]

However, by material specific tailoring, hot cracks can be avoided. By addition of appropriate alloying elements or fine dispersed ceramic particles acting as nuclei, hot cracks can be suppressed by forming a fine grained microstructure since a lot of crystallization seeds are formed in the melt. [6] As a consequence, the distance between the solidifying nuclei is low and the thermal tensions are lower and relieved over short distances.

2. Theoretical Considerations and used Equipment

The energy density in the cross section of the laser spot at the surface level depends on the optics setup like the focal length and optical fiber used as well as on the melting temperature or melting range and heat conductivity of the material. It is responsible for the geometric shape and quality of the weld seam formed by laser welding.

2.1   Impacts of Material Properties

Together with an expansion of the melting range and a shifting towards lower temperatures, alloying elements have a strong impact on the heat conductivity compared to pure aluminum (Table 1, Figure 1). A wide melting range is responsible for bad weldability and sensitivity of a material to hot cracks. [7]

Table 1:   Heat conductivity for selected aluminum alloys according to [8]

alloy	EN-No.	Heat conductivity at room temperature [W/m*K]	Melting point or range [°C]	ΔT_S [K]
Al99.98	AW-1098	215-227	660	0
AlMg3	AW-5754	140-160	610-640	30
AlMgSi1	AW-6082	170-220	585-650	65
AlCuMg1	AW-2017A	130-200	515-640	125

2.2   Technological Influences

Also technological parameters like the position of the focal point in relation to the surface and the depth of the focus, depending on the focal length and aperture, may influence the result strongly (Equation 1). In practice, it is easier to control the position of the focal point instead of maintaining or varying the energy density. According to Figure 3 and depending on the focal length, the cross section and hence the energy density can be calculated for different optical fibers taking $2*w_0$ as the fiber diameter for a given focal length.

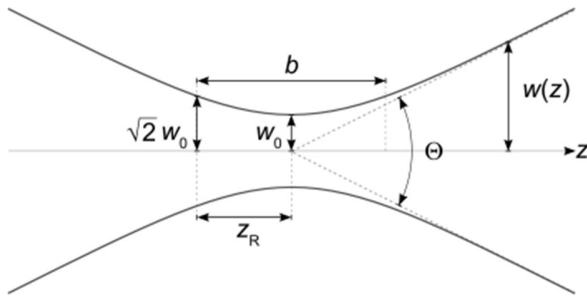$$tan\frac{\Theta}{2} = \frac{w_{(z)}}{z}$$ **Equation 1**

Figure 3: Definition of the Rayleigh length z_R and its dependence of the focal length

For laser welding a TrucCell 3010 machine combined with a TruDisk 3001 laser by TRUMPF was used. The disk laser was equipped with two fiber connectors and could be coupled with a 100 µm and a 400 µm optical fiber, respectively. The collimation had a focal length of 150 mm. According to [9] the diameter of the beam after the collimation d_{fc} is 33 mm. It was used together with lenses BEO D70 with a focal length of 150 mm. This gives a beam angle of 6.277° per side. From this, the cross section on the surface level was calculated depending on the focal position (Figure 4) according Table 2. To reach the so called deep-welding effect, an energy density of roughly 1 MW/cm² is necessary to form a stable plasma keyhole. [10] It turns out, that the percentage drop of the energy density at the surface level is much more pronounced for the 0.1 mm-fiber than for the 0.4 mm-fiber.
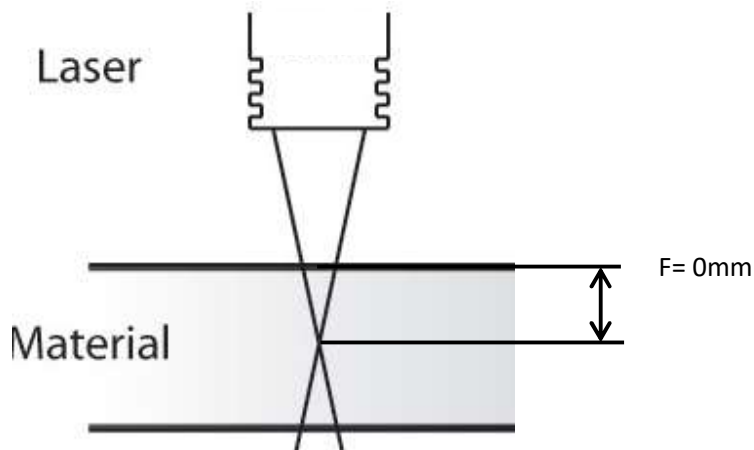

Figure 4: Fluctuating energy density at the surface according the position of the focal point

For negative focal points inside the material, the highest energy density is below the surface. For focal points above the surface there is the same energy density at the surface level as for negative focal points. However, less energy is converted into heat since the focal point is above the material and the hot spot is not inside the material. From this, the results are expected to be different for the same defocussing, positive and negative, respectively.

Table 2: Influence of the focal position and optical fiber on the energy density at the surface level for $d_{fc}/2$ = 16.5 mm and a focal distance of f=150 mm

	For Fiber-Ø 0.1 mm				For Fiber-Ø 0.4 mm			
Position F of the focal point related	Diameter at surface	Cross section	energy density for	percentage drop related	Diameter at surface	Cross section	energy density for	percentage drop related

to the sample surface [mm]	[mm]	[mm2]	P= 3 kW [MW/cm²]	to position above [%]	[mm]	[mm2]	P= 3 kW [MW/cm²]	to position above [%]
0	0.1	0.007854	38.197		0.4	0.125664	2.387	
-1	0.32	0.080425	3,73	-90.2	0.62	0.301907	0.994	-58.4
-2	0.54	0.229022	1,31	-64.9	0.84	0.554177	0.541	-45.6
-3	0.76	0.453646	0.661	-49.5	1.06	0.882473	0.34	-37.2

For an optical fiber of 0.1 mm diameter, deep welding should occur also for a focal position of -2 mm. However, for a fiber with 0.4 mm diameter, deep welding is hardly achieved even for a focal position of -1 mm.

For laser welding of highly thermally conductive materials, such as aluminum, the impact of power and focal position is huge.

3. Experiments and Interpretations

For all welding experiments 15 l/min of Ar 5.0 was supplied by a single nozzle aligned in front of the welding direction for shielding of the melt. A length of 20 mm was welded for each set of parameters. Afterwards, the samples were cut into pieces perpendicular to the weld seams using a cutting machine "Brillant 250" by ATM and a 300 mm disk, type C with a width of 2 mm. Then, both half of the samples were roughly grinded by hand with 600 grid abrasive paper using a grinding machine "Saphir 550" by ATM and were finally etched using 2 % KOH-solution. By this means, a coarse development of the metallografic microstructures were obtained allowing the verification of the molten cross section due to different chemical attack of semi manufactured and rapid solidified material. Photographs were taken from both sides of all samples, meaning the weld seam pictures had a distance of at least 2 mm from the disk of the cutting machine plus grinding. Both pictures were evaluated to prove that results are identically and to prevent misinterpretation. However, it should be kept in mind that the results show local details and that a large number of analyses is required to obtain a realistic picture. Especially for perfect weld seams more experiments should be done to prove that the weld seam is free of any pores.

3.1 For AlMg3

AlMg3 sheets of 3 mm thickness were welded with both, pulsed as well as continuous wave (cw) mode. For all pulsed mode welding seams, cracks were observed at the surface. Hence, pulsed mode welding was not investigated in detail anymore.

For cw-mode, welding tests were performed using different power and focal position with both, optical fibers of 0.1 mm and 0.4 mm diameter, respectively. All experiments were conducted with a velocity of 3 m/min since for lower speed, e.g. 1 m/min, the weld seam is strongly influenced by heat conduction.

For the 0.4 mm fiber and a power of 2 kW (Figure 5), the cross section of all weld seams is triangular and seems to be dominated by the high heat conduction of the material. No distinct increase of the welding depth with deeper position of the focal point could be found. A weak maximum of the welding depth is found for F= -1 mm. In fact, there was no strong effect on the welding depth at all, probably due to the large cross section of the laser beam and the low energy density.

From this, it is obvious, that less power would have no desirable effect. Obviously, the melt formed seem to have a smooth temperature profile across the whole cross section without zones of overheating. Only a few small pores were observed.
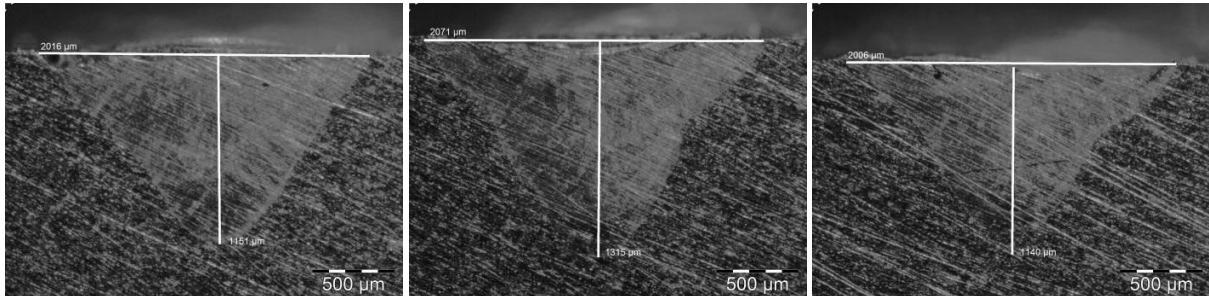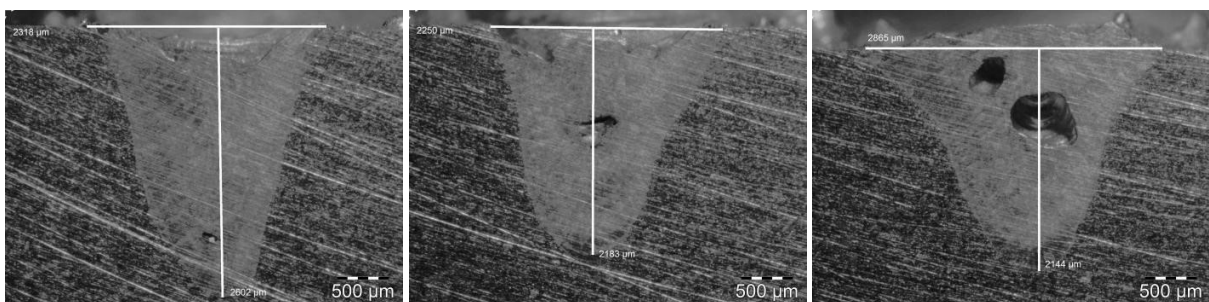

Figure 5: Laser weld seam of AlMg3 using a 0.4 mm optical fiber, P=2kW, v= 3 m/min, from left to right: F= 0, -1 and -2 mm, respectively.

For the same variations of the position of the focal point, the maximum welding depth for a power of 3 kW was achieved for F= 0 mm (Figure 6). Obviously, for 3 kW the power input exceeds the heat conductivity. The shape of the weld seam indicates deep welding.

The deeper the position of the focal point, the more the energy density at the surface level drops. As a consequence, the melt at the surface solidifies before the overheated melt below does. A lot of big shrink pores were formed by thermal contraction. This occurred also for F= -1 mm, where the energy density is near 1 MW/cm² according Table 2 at the surface and illustrates, that this value is not a panacea for deep welding of all materials and other involved parameters <u>especially regarding welding velocity and heat conductivity of the material</u>.

Fewest pores were observed for F= 0 mm since melt in the depth was formed only by heat conduction and no overheating occurred. For F= -2 mm the 3 kW are not sufficient to increase the welding depth compared to F= -1 mm, however, the pore formation is reinforced.

Figure 6: Laser weld seam of AlMg3 using a 0.4 mm optical fiber, P=3kW, v= 3 m/min, from left to right: F= 0, -1 and -2 mm

For the 0.1 mm optical fiber the results are different: Even for a power of 1 kW (Figure 7) there is a pronounced maximum of the welding depth at F = -1 mm. For the 0.1 mm-fiber, the energy density is much higher and reaches at the surface level still 3.73 MW/cm² for F= -1 mm. The shape of the weld seam turns more to deep welding. However, the power is still too low and some small pores are formed. The same happens for F= -2 mm: There is not enough energy input into the depth of the material, and

6

the welding depth decreases. However, no shrink pores are formed, probably because the energy is dissipated completely.
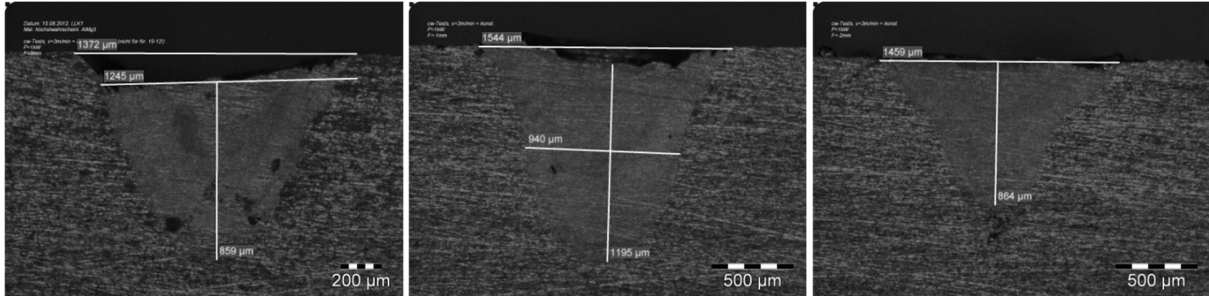
Figure 7: Laser weld seam of AlMg3 using a 0.1 mm optical fiber, P=1kW, v= 3m/min, from left to right: F= 0, -1 and -2 mm

For 2 kW (Figure 8) first the welding depth increases with greater depth of the focal point related to the material surface: The energy density for the 0.1 mm-fiber is high enough to dominate the heat conduction regardless of the position of the focal point related to the surface. Also for F= -2 mm, the energy density at the surface is still 1.31 MW/cm², and the high heat conductivity will help, too. However, since the melt in the depth is strongly overheated and the molten area generated at the surface is too low for 2 kW power, shrink pores are formed for all depths of the focal point because the melt solidifies at the surface first.
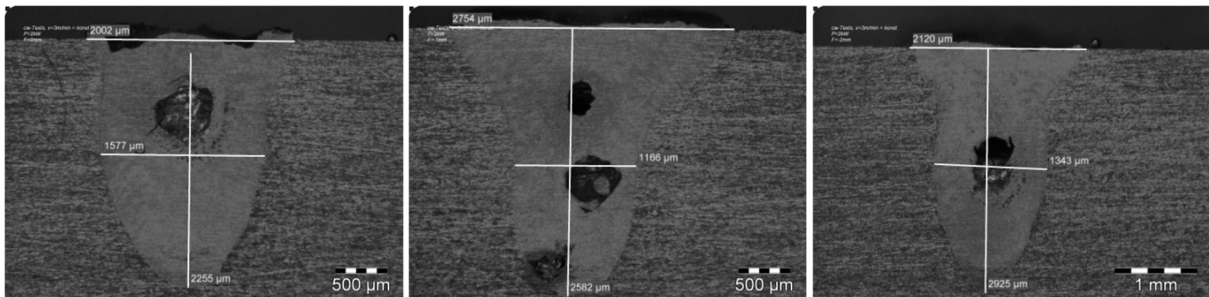
Figure 8: Laser weld seam of AlMg3 using a 0.1 mm optical fiber, P=2kW, v= 3m/min, from left to right: F= 0, -1 and -2 mm

Finally, a power of 3 kW was applied (Figure 9). Differences of the cross sections for all focal depths are visible; however, the increase of the welding depth is not as pronounced as for a power of 2 kW. In fact, between F= 0 mm and F= -1 mm no difference of the welding depth is visible, except that the width of the weld seam at the surface is strongly increased for F= -1 mm. Surprisingly, only a few small pores are visible for F= -1 and -2 mm: Both weld seams show the typically nail-shaped cross section for deep welding despite the high heat conductivity of the material. The width of the weld seams at the surface is strongly increased for F= -1 mm, followed by a slim neck. A possible explanation is that much more melt is formed for 3 kW than for 2 kW. In turn, the solidification of the melt at the surface is retarded compared to 2 kW and no shrink pores are formed. For F = -2 mm, the width of the weld seam at surface level is reduced compared to F= -1 mm. Obviously, the energy density at the surface is too low <u>due to the lower position of the focal point</u>, so the heat conductivity prevents the formation of a broader melt. The relation between heat conductivity and the molten cross section allows solidifying without freezing at

the surface first. Hence, nearly no shrink pores are formed <u>but the welding depth is increased moderately compared to F=-1 mm.</u>
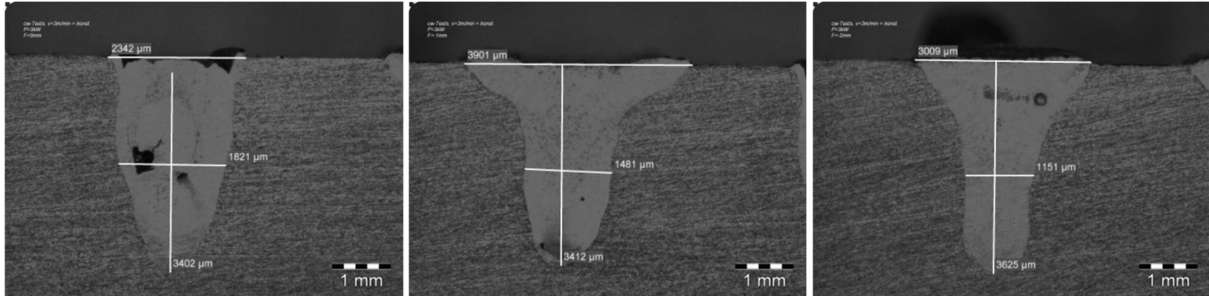
Figure 9: **Laser weld seam of AlMg3 using a 0.1 mm optical fiber, P=3kW, v= 3m/min, from left to right: F= 0, -1 and -2 mm, respectively.**

3.2 Spray-compacted Hypereutectic Aluminum Alloys

According to the binary Al-Si-phase diagram displayed in Figure 10, above the eutectic point at 12.6 wt.-% silicon coarse Si-grains are precipitated primarily from the melt. [11] Simultaneously, the composition of the remaining melt drops with decreasing temperature to the eutectic point. Finally, the rest of the melt solidifies at the eutectic composition as grains with intragranular lamellas of α-Al and silicon. Depending on the relation between solidified silicon and eutectic, no whole grains but seams of the eutectic between solidified and brittle silicon grains may be formed. Additionally, with increasing silicon content the solidification range is extended, a predestinated state for hot cracks. Whereas a metallographic microstructure consisting of 100 % eutectic grains has favorable mechanically properties, the mixture of brittle silicon grains together with grains of the eutectic won`t. Eutectic 12 % Si-aluminum alloys are widely used for master forming by casting as an energy-efficient material with a low melting temperature and exhibiting good mechanical properties as well.

<u>Binary phase diagrams are valid only for the thermodynamically equilibrium. In engineering, however, nonequilibrium conditions like technologically useful cooling rates are applicable. This may alter the materials microstructure. E.g. for an eutectic, the thickness of as well as the distance between the lamellas formed depend on the cooling rate, representing the available time for diffusion during the decomposition of the homogenous melt. Eventually, spray-compacting represents a rapid cooling technology able to stabilize metastable conditions of solid solutions by freezing.</u>

<u>The more metals in addition to aluminum and silicon are present in an alloy, the more complex becomes the phases possibly formed in ternary or quaternary systems.</u>
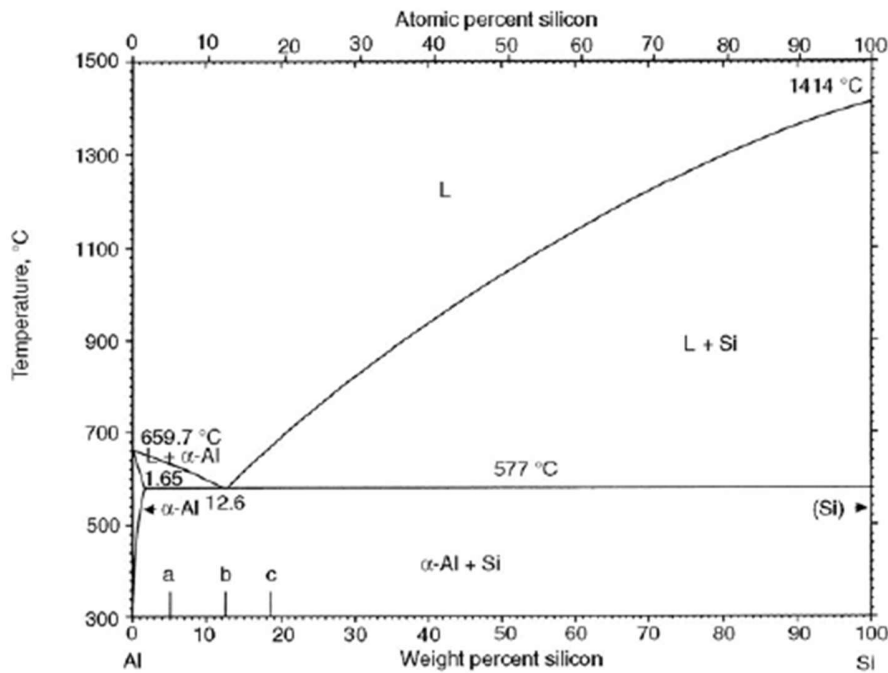
Figure 10: Binary phase diagram of Al-Si [11]

Hypereutectic alumina alloys can be fabricated via departure from the thermodynamically equilibrium through rapid solidification, predominantly suppressing the primary crystallization of silicon leading to a metastable microstructure. E. g. PEAK Werkstoff GmbH in Velbert, produces different grades of hypereutectoid aluminum alloy by spray-compacting: The molten material is atomized by nitrogen and deposited as small droplets onto a rotating plate, reaching high solidification rates. [12, 13] Afterwards, the sprayed billet is extruded for compaction reasons and for getting the ride shape, since the formation of small pores between the single droplets cannot be avoided completely during spray-compacting.

Spray-compacted hypereutectic DISPAL®-aluminum alloys were supplied by PEAK Werkstoff GmbH as extruded round stock of different diameters, ranging from 50-90 mm. Disks with a thickness of more than 4 mm were cut off using the "Brillant 250" cutting machine by ATM. Both sides were ground using 600 grain abrasive paper and the "Saphir 550" grinding machine.

Three alloys with different silicon contents were investigated: DISPAL® S232 (AlSi17Fe4Cu2.5MgZr), DISPAL® S250 (AlSi20Fe5Ni2) and DISPAL® S225 (AlSi35Fe2Ni). Since the alloy with 20 % silicon contains some other elements too, DSC measurements were performed to characterize the melting interval (Figure 11, Table 3). The measurements were performed using a Netzsch 404 C Pegasus thermal analyzer and a heating rate of 10 K/min was applied. The investigated temperature range was 100 to 850°C. At this temperature, also an alloy containing 35 % silicon should be completely in the molten state. The crossing point of the tangents at the inflection point of inflexion and the base line was taken as the beginning of a melting peak (onset temperature).
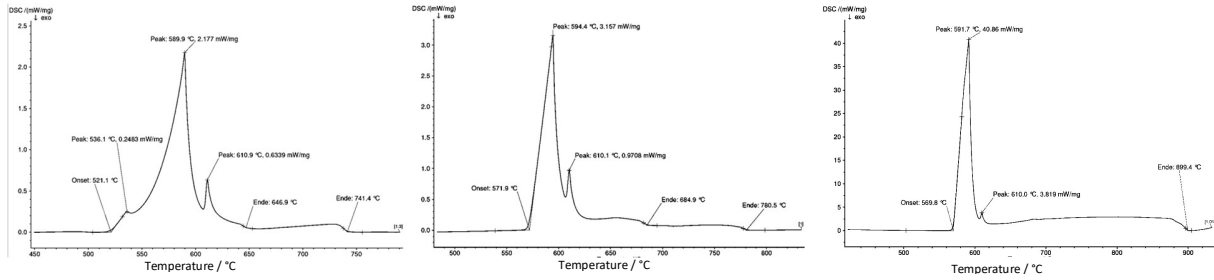
Figure 11: From left to right: DSC-measurements of DISPAL® S232 (AlSi17Fe4Cu2.5MgZr), DISPAL® S250 (AlSi20Fe5Ni2) and DISPAL® S225 (AlSi35Fe2Ni), respectively

Table 3: Overview about the melting peak temperatures measured by DSC for AlSi17Fe4Cu2.5MgZr, AlSi20Fe5Ni2 and AlSi35Fe2Ni

alloy	PEAK-nomenclature	T_s-Range [°C]	Peak Temperature 1 [°C]	Peak Temperature 2 [°C]	Peak Temperature 3 [°C]
AlSi17Fe4Cu2.5MgZr	DISPAL® S232	521-741	536	590	611
AlSi20Fe5Ni2	DISPAL® S250	572-780	594	610	
AlSi35Fe2Ni	DISPAL® S225	570-899	592	610	

Also other physical properties like the heat conductivity and the coefficient of thermal expansion are significantly lowered compared to AlMg3 (Table 4) affecting the susceptibility for hot cracks.

Table 4: Physical properties of AlMg3 and different DISPAL®-alloys, respectively

| alloy	PEAK-nomenclature	Heat conductivity [W/m*K]	Coefficient of thermal expansion [10-6/K]	Density [g/cm³]
AlMg3		130-140	24	2.7
AlSi17Fe4Cu2.5MgZr	DISPAL® S232	117	18.4	2.79
AlSi20Fe5Ni2	DISPAL® S250	123	16.9	2.78
AlSi35Fe2Ni	DISPAL® S225	127	15.1	2.58

EDS measurements were performed using a microprobe JXA-8530-F by JEOL for weld seams made with the parameters P= 3 kW, F= -1 mm and v= 5 m/min to determine the different phases visible by back scattered electrons for all materials. As detector a SDD was used. The working distance was 11 mm. An acceleration voltage of 15 kV was used and 100 s life time for measuring.

3.1.1 For AlSi17Fe4Cu2.5MgZr (DISPAL® S232)

The weld depth and the width at the surface as well as at half of the welding depth are reduced with increasing velocity for both positions of the focus (Figure 12). Shifting the focal position from the surface level to 1 mm inside the material, the welding depth is increased significantly. Also the width of the weld at half of the welding depth is decreasing. Increasing depth of the focal position and increasing velocity help to prevent shrink pores.

For a velocity of 3 m/min and a decrease of the focal point, the width of the welding seam at the surface is increased whereas it is reduced at higher velocities. This effect increases the higher the velocity is and shows that for lower velocities the impact of the heat conduction increases.

For velocities beyond 10 m/min the power of 3 kW may be too low. However, higher speed may lead to narrower weld seams at the surface.
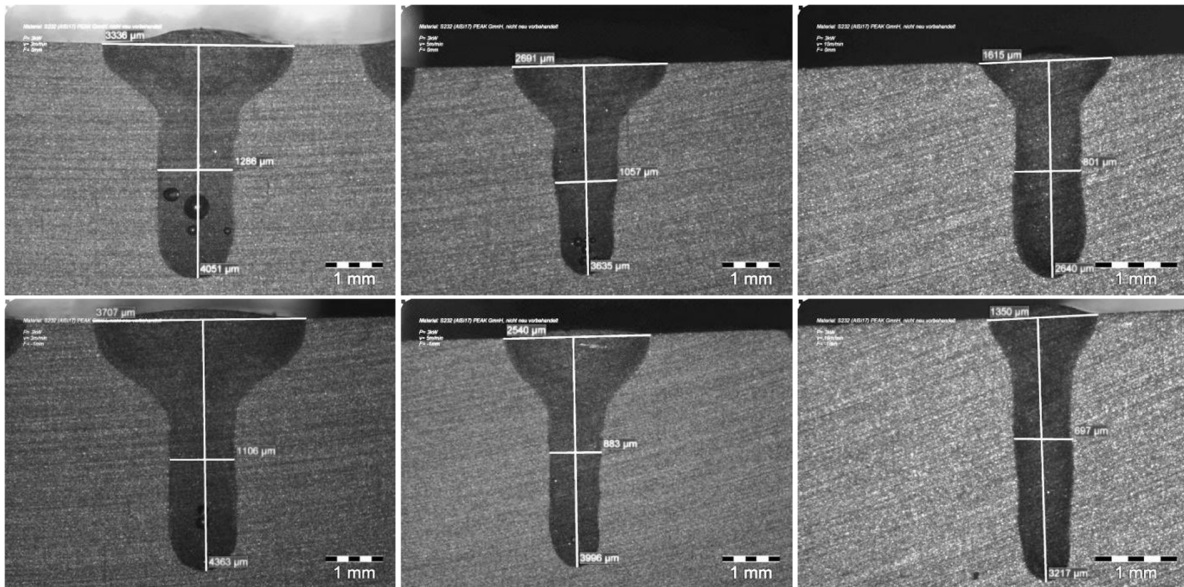
Figure 12: Dependence of the weld seam for AlSi17Fe4Cu2.5MgZr on velocity. P= 3 kW. Top: F = 0 mm; below: F= -1 mm. From left to right: welding velocities of 3; 5 and 10 m/min, respectively.

Investigations by EDX were focused on weld seams conducted with P= 3 kW, F= -1 mm and v= 5 m/min. Already in the BSE-SEM-pictures, several phases indicated by different grey levels could be distinguished. Figure 13 shows an overview about the welding zone with a concentration of spicular precipitations in the center of the weld seam according to the local cooling conditions and colling rates.

Generally, alloying elements like iron and copper are concentrated in a few minor precipitations. Due to the rapid solidification during spray-compacting, the shape is more rounded, and less irregular precipitations are found (Figure 14).

The morphology of the precipitations change drastically from the as-delivered state to the weld seam: Inside the welded area, especially in the center where the solidification is most retarded, spicular silicon precipitations are formed but also irregularly precipitates are present (Figure 15). The shape and dimension of the precipitations depend on the composition as well as on the local cooling rate. In the heat affected zone at the transition to the as-delivered state and in the center of the weld seam the cooling rate is the lowest and the longest needles possessing remarkable aspect ratios are formed. Especially precipitations rich in aluminum, silicon and iron (Table 5, spot 2 of the as-delivered state and spot 1 in the weld seam) tend to form its shape to spicular whereas Cu-rich precipitates containing less silicon and iron (Table 5, spot 1 of the as-delivered state and area 4 in the weld seam) change to reticular shape. Of course also the welding velocity and the composition of the alloy will have a strong impact on the shape and dimension of the precipitates.
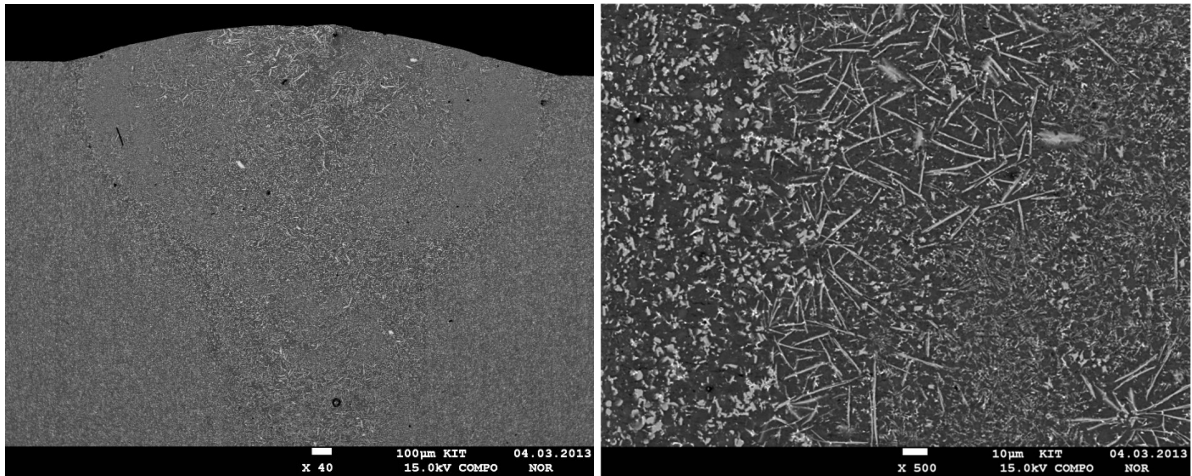
Figure 13: Left: BSE-SEM-overview of the weld seam of AlSi17Fe4Cu2.5MgZr. Right: Higher magnification of the transient area from the as-delivered material to the weld seam.
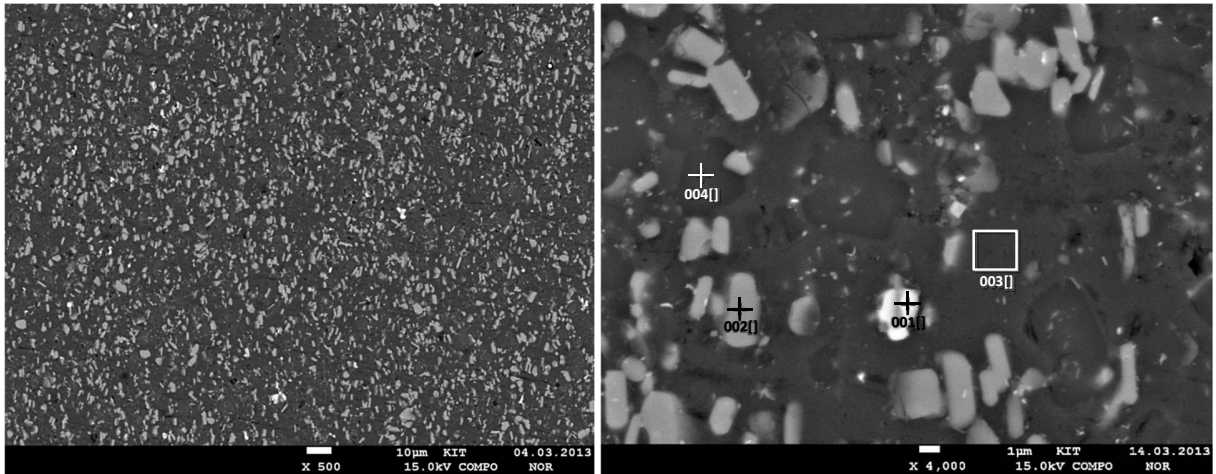

Figure 14: BSE-SEM-picture of the microstructure of the as-delivered-state of AlSi17Fe4Cu2.5MgZr
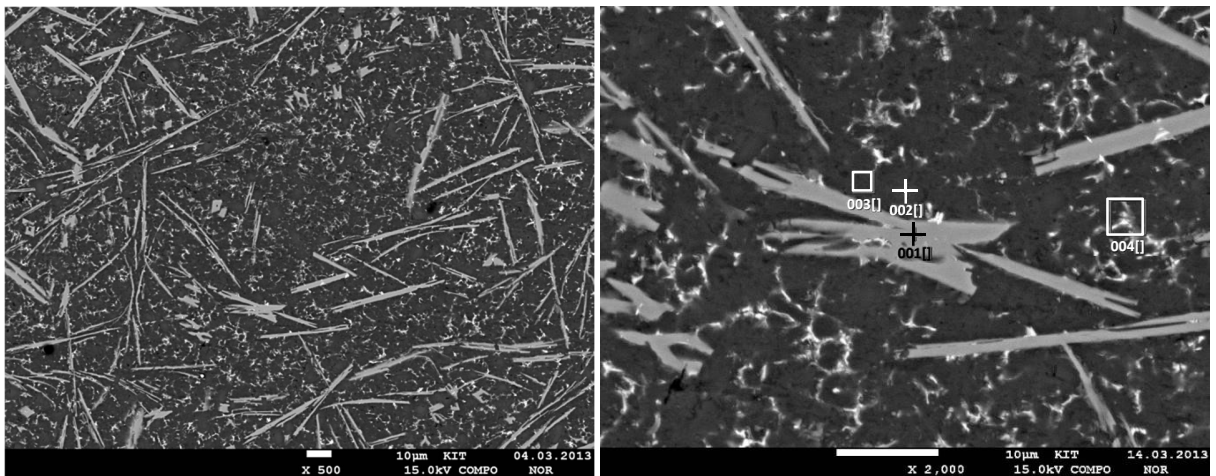

Figure 15: BSE-SEM-picture of the microstructure of the weld seam of AlSi17Fe4Cu2.5MgZr

EDS-measurements were performed on both areas, the as-delivered state and inside the weld seam. Three to four different phases could clearly be distinguished.

In the as-delivered state, some phases consisting mainly of silicon and with very low aluminum content are formed. Obviously, the stirring of the melt during laser welding together with high solidification rates prevent the formation of very aluminum-rich phase as well as of phases containing very low aluminum and high silicon contents (Table 5).

Table 5: **EDS-analysis of AlSi17Fe4Cu2.5MgZr with results in wt.-%. Table left: As-delivered state (Figure 14, right). Table right: Weld seam (Figure 15, right).**

Element	O	Mg	Al	Si	Fe	Cu	O	Mg	Al	Si	Fe	Cu
001	1.66	0.27	82.61	3.91	5.94	5.61	1.54		45.73	26.78	25.94	
002	1.28	0.09	66.01	15.17	16.53	0.93	3.27	0.13	49.80	45.15	0.88	0.77
003	1.32	0.31	92.71	1.65	0.80	3.22	1.19	0.14	83.29	12.70	1.47	1.20
004	0.40		4.78	93.94	0.23	0.64	1.46	1.66	74.02	13.93	2.17	6.76

3.1.2 For AlSi20Fe5Ni2 (DISPAL® S250)

Weld seams in materials possessing higher silicon contents and additional alloying elements lead to enhanced pore formation. The reason is that despite high solidification rates, the temperature range of solidification is extended.

The width of the weld seam at the surface depends not as clearly on the focal position and does not follow the same trend as for AlSi17Fe4Cu2.5MgZr (Figure 16). Also for a velocity of 5 m/min the width at the surface still increases and is not decreased for 10 m/min. As opposed to AlSi17Fe4Cu2.5MgZr, the width at half of the welding depth is increased for velocities of 3 and 5 m/min for the focal position at -1 mm. Only for 10 m/min it is nearly identically. Pores appear for all parameters, also for higher velocities.
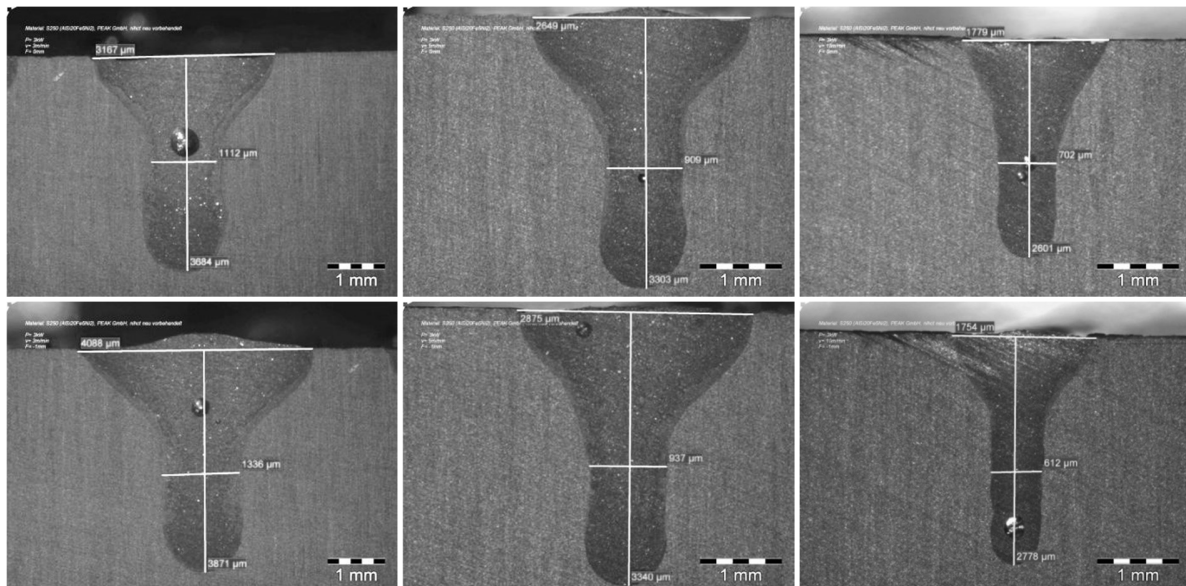
Figure 16: Dependence of the weld seam for AlSi20Fe5Ni2 on velocity. P= 3 kW. Top: F = 0 mm; below: F= -1 mm. From left to right: welding velocities of 3; 5 and 10 m/min, respectively.

Again, BSE-SEM-pictures were made to distinguish the different phases formed in the material. Figure 17 gives an overview about the cross section and the transition area to the as-delivered state.

The precipitation density in Figure 17 and Figure 18 is higher compared to AlSi17Fe4Cu2.5MgZr. The iron- and the silicon-rich phases (Table 6) in the as-delivered state (Figure 18) show small cracks from rapid cooling during spray-compacting. Especially the latter one is supposed to be very brittle due to its high silicon content. However, no phase can be allocated since silicon has no solubility for aluminum and vice versa (Figure 10). The density of voids seems to be less in the weld (Figure 19). Three different phases could be detected in the as-delivered as well as in the as-welded state. No effect suppressing any specific phase by the dynamics during welding like for AlSi17Fe4Cu2.5MgZr was found. In the as-welded state, nickel seems to be distributed more homogeneously.
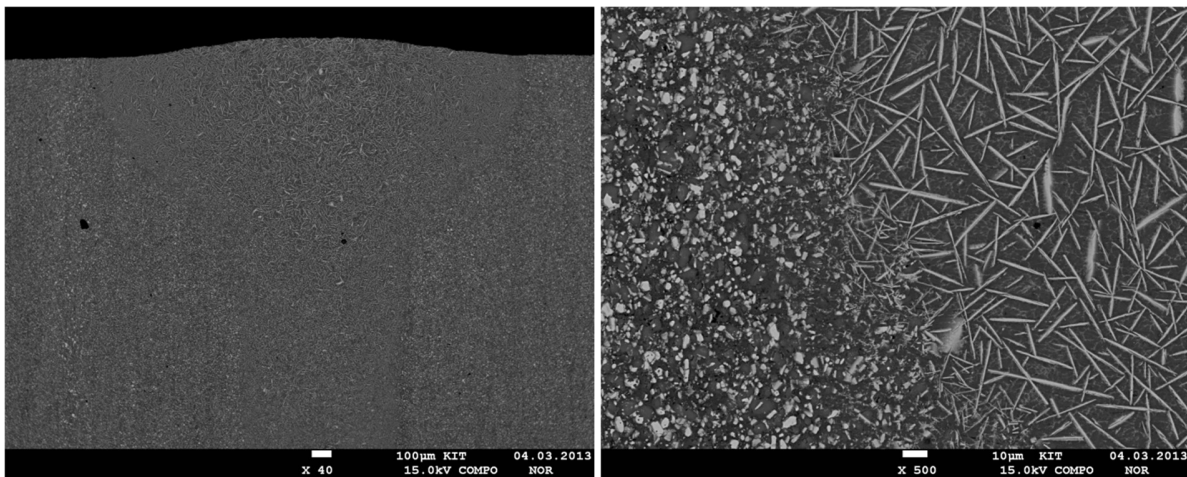
Figure 17: Left: BSE-SEM-overview of the weld seam of AlSi20Fe5Ni2. Right: Higher magnification of the transient area from the as-delivered material to the weld seam.
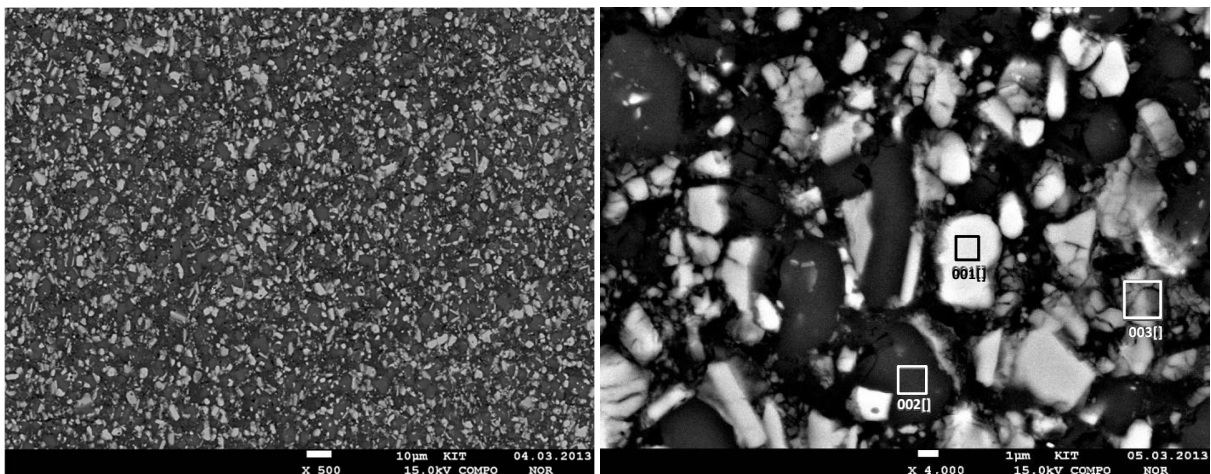
Figure 18: BSE-SEM-picture of the microstructure of the as-delivered-state of AlSi20Fe5Ni2
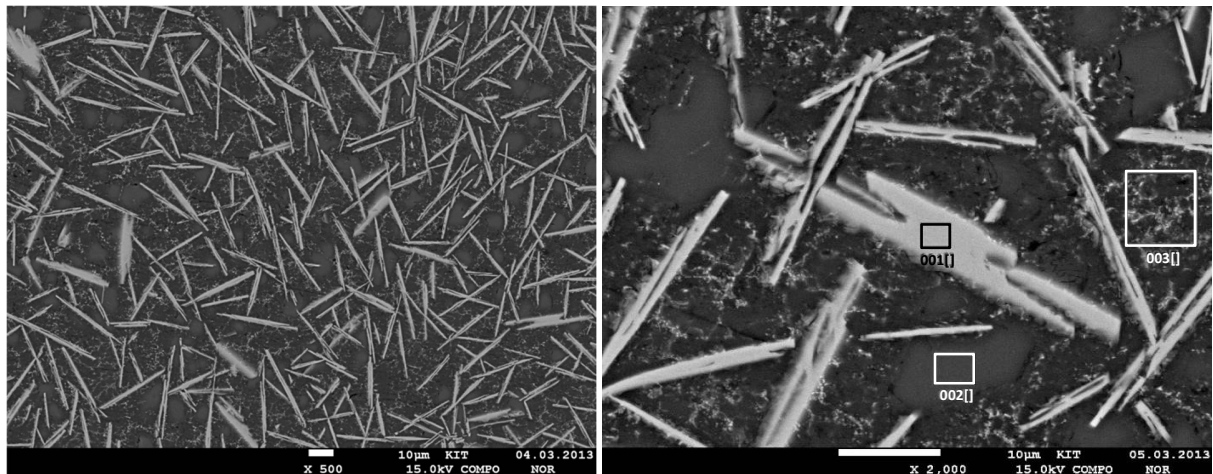
Figure 19: BSE-SEM-picture of the microstructure of the weld seam of AlSi20Fe5Ni2

Table 6: EDS-analysis of AlSi20Fe5Ni2 with results in wt.-%. Left: As-delivered state (Figure 18, right). Right: Weld seam (Figure 19Figure 15, right).

Element	O	Al	Si	Fe	Ni	O	Al	Si	Fe	Ni
001	1.68	66.93	3.72	13.77	13.91		46.76	25.22	25.84	2.18
002	0.80	26.19	72.99		0.02	1.17	15.19	83.39		0.26
003	2.88	84.15	5.21	6.99	0.77	1.82	82.04	11.69	1.04	3.41

3.1.3 For AlSi35Fe2Ni (DISPAL® S225)

The cross sections of weld seams in AlSi35Fe2Ni (Figure 20) shows the same trends like described for AlSi20Fe5Ni2(Figure 16). Some pores occur but for the highest velocity of 10 m/min.
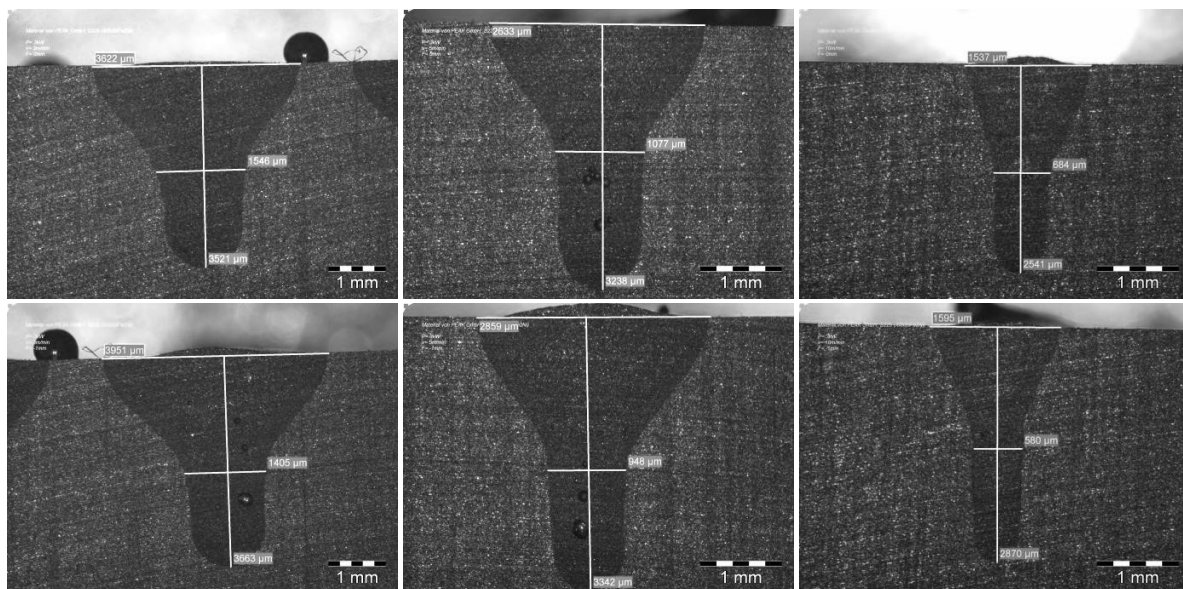

Figure 20: Dependence of the weld seam for AlSi35Fe2Ni on velocity. P= 3 kW. Top: F = 0 mm; below: F= -1 mm. From left to right: 3; 5 and 10 m/min, respectively.

Already the overview of the welded sample (Figure 21) looks different: less spicular but irregular and dendritic precipitations are formed. The EDS-analysis of a rectangular area in this area will be an average of different phases.

Due to the high silicon content of 35 % the density of precipitations is even higher than for AlSi20Fe5Ni2. In the as-delivered state (Figure 22), cracks inside the silicon-rich phase (Table 7) and small voids across the material can be seen. <u>This may arise from the extrusion of the spray-compacted cones by with a high degree of natural strain and the brittleness of the silicon-rich phase.</u> In the weld seam (Figure 23), the morphology of silicon-rich precipitations is irregular and coarsened. No cracks in the silicon-rich phase are visible. The most voids are cured.
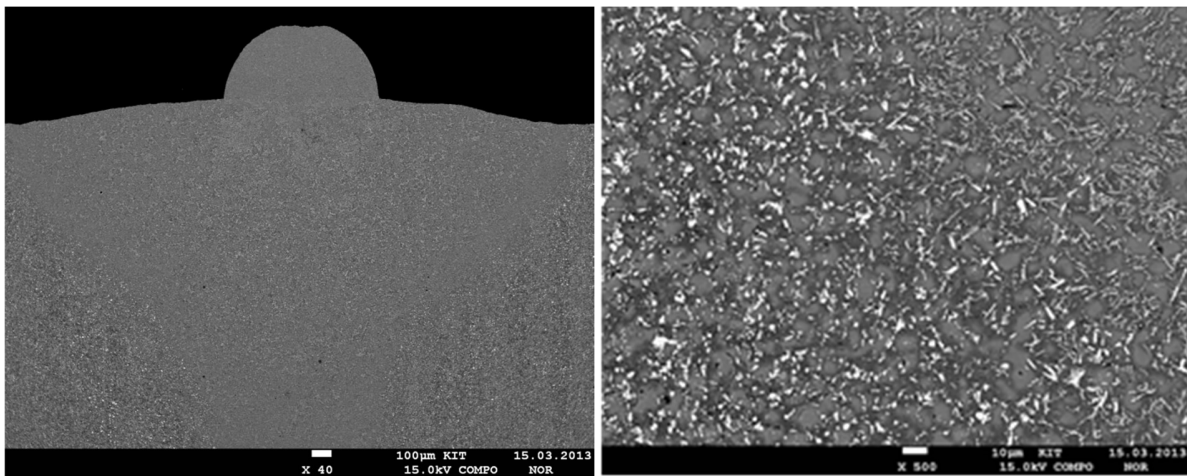

Figure 21: Left: BSE-SEM-overview of the weld seam of AlSi35Fe2Ni. Right: Higher magnification of the transient area from the as-delivered material to the weld seam.
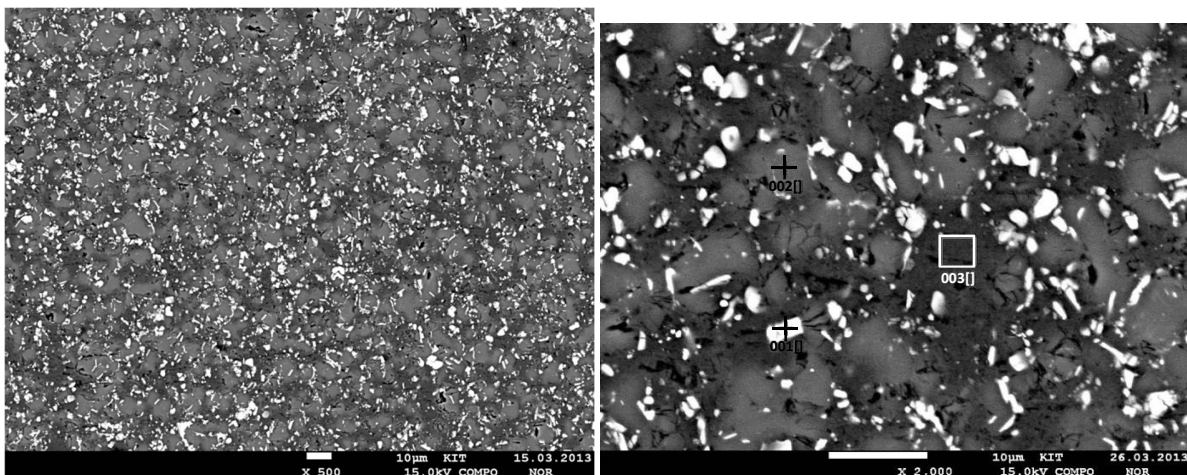

Figure 22: BSE-SEM-picture of the microstructure of the as-delivered-state of AlSi35Fe2Ni.
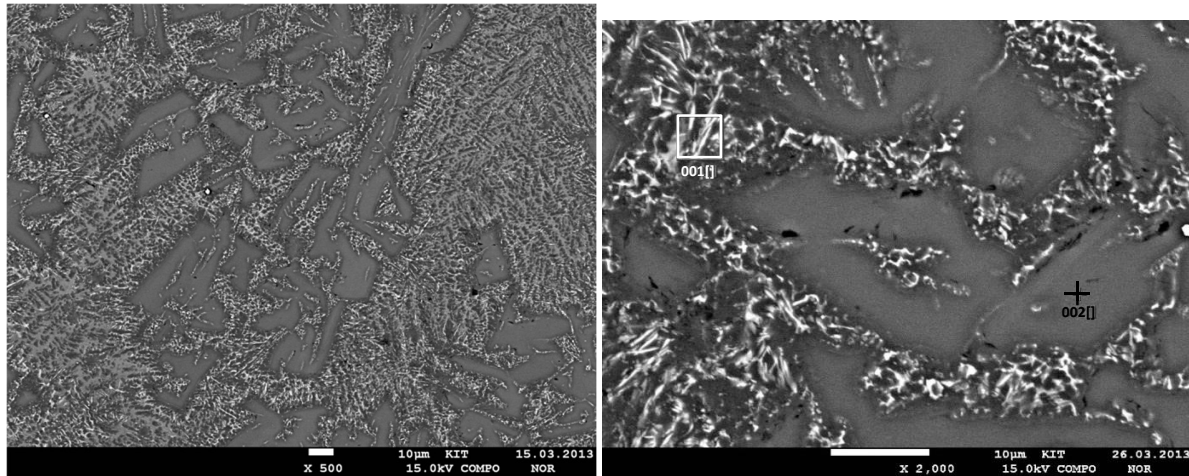
Figure 23: BSE-SEM-picture of the microstructure of the weld seam of AlSi35Fe2Ni

Table 7: EDS-analysis of AlSi35Fe2Ni with results in wt.-%. Table left: As-delivered state (Figure 22, right). Table right: Weld seam (Figure 23, right).

Element	O	Al	Si	Fe	Ni	Cu	O	Al	Si	Fe	Ni	Cu
001	1.72	89.07	6.96	1.43	0.81		1.54	78.95	12.26	4.43	2.50	0.32
002	0.57	3.67	95.38	0.30	0.09		0.35	22.63	76.03	0.42	0.23	0.34
003	1.93	95.40	1.24	0.59	0.42	0.42						

4. Conclusion

The experiments described show that the success of welding aluminum alloys depends on a lot of parameters. Namely a sufficient energy density at the surface level is necessary for obtaining deep weld seams without pores. Only with the 0.1 mm light-conducting cable a sufficient energy density for deep welding can be achieved. The value of 1 MW/cm² for the formation of the deep welding effect is not a panacea for all materials. From the experiments on AlMg3 it can be concluded, that the energy density should be 2-3 MW/cm² at the surface level. The necessary energy density for deep welding seems to be influenced mainly on the thermal conductivity of a material. This has also to be considered in subject to the welding velocity.

Additionally, it has to be kept in mind that even low percentages of alloying elements alter the heat conductivity of aluminum drastically. Especially the welding power should be correlated taking into account the heat conductivity of each alloy. Higher welding velocities seem to be helpful to control the dissipation of the energy at high heat conductivities. For aluminum alloys in general a power of several kilowatts is necessary to achieve deep welding. If a very high melting point, e.g. like for tantalum, has a similar impact on the formation of weld seams is not clear yet.

A power of 3 kW can be considered to be the lower limit to weld materials possessing a high thermal conductivity at reasonable welding velocities. Higher power might be needed to increase the welding speed and to take advantage of the high process velocity of laser welding.

For deep weld seams, thin light-conducting cables leading to a high energy density at reasonable power are necessary for materials possessing a high thermal conductivity. However, there are technological limits since the thinner the light-conducting cable the more difficult is it to bridge gaps or to obtain a sufficient width of the weld seam without overheating of the melt locally, promoting the formation of pores.

As known from literature, for aluminum it is difficult to achieve weld seams without pores. However, in the experiments described for AlMg3, pore formation is more attributed to thermal shrinkage after the solidification started at the surface first, than to hydrogen formation and its drastically lowered solubility in aluminum during the solidification.

For micro process engineering, the most commercial aluminum alloys appear to be not suited to manufacture high vacuum proof apparatuses made of thin sheet material. Also the corrosion resistance required by an application can be in contradiction to the weldability.

Due to the high thermal conductivity, also the crystal morphology of hypereutectic aluminum alloys will be influenced by the welding velocity and hence varying cooling rates. Additional alloying elements besides silicon affect the shape and size of the precipitations formed.

With increasing silicon contents and additional alloying elements the solidification range is extended and increased to higher temperatures. The morphology and density of precipitations as well as voids in the spray-compacted and the as-welded state depends mainly on the silicon content. Especially the spicular precipitations in AlSi17Fe4Cu2.5MgZr and AlSi20Fe5Ni2 depend according their position and the local cooling rate of the weld seam.

In general, the cross section of weld seams of aluminum alloys depend strongly on:

1. The heat conductivity of the chosen alloy,
2. the optical fiber used,
3. the focal position relatively to the surface,
4. the power and
5. the welding speed

Items 2, 3 and 4 will define the power density at the surface level. For defect-free weld seams the interaction of all the parameters mentioned above have to be taken into account.

All welding experiments were made on solid materials. For joining of parts made of hypereutectic aluminum alloys investigations using a scanner should be performed to widen the melting zone and to investigate its effect on the shrink behavior. However, if the molten area is widened the velocity has to be reduced changing the whole complex temperature distribution of the weld.

The mechanically properties of welding zones of hypereutectic aluminum alloys concerning yield and tensile strength, strain to rupture as well as fatigue strength should be evaluated in comparison to the spray-compacted as-delivered material.

Acknowledgement

Literature

[1]   W. Gref, *Laserstrahlschweißen von Aluminiumwerkstoffen mit der Fokusmatrixtechnik*, Herbert Utz-Verlag Wissenschaft, Munich, pp. 26, **2005**

[2]   S.-F. Goecke, *Auswirkungen von Aktivgaszumischungen im vpm-Bereich zu Argon auf das MIG-Impulsschweißen von Aluminium*, graduate thesis, TU Berlin, **2004**

[3]   M. Wolf, *Zur Phänomenologie der Heißrissbildung beim Schweißen und Entwicklung aussagekräftiger Prüfverfahren*, graduate thesis, Universität Hamburg, BAM-Dissertationsreihe Vol. 19, **2006**

[4]   L. Baum, V. Fichtner, *Der Schutzgasschweißer - Teil2: MIG-, MAG-Schweißen*, DVS-Media GmbH, vol. 12, 3rd. Ed., Düsseldorf, **1990**

[5]   U. Dilthey, *Schweißtechnische Fertigungsverfahren 2*, 3rd. Ed., Springer, Berlin, Heidelberg, New York, ISBN 3-540-21674-X, p. 234, **2003**

[6]   T. Seefeld: „Verbesserung der Schweißeignung von Aluminium durch geeignete Schweißzusatzstoffe", Lasermagazin, pp. 68-69, Mai **2011**

[7]   H. Waldmann *Werkstoffliche Aspekte des Laserstrahlschweißens von Aluminiumlegierungen für den Fahrzeugbau*, Ed. H. W: Bergmann, G. Ziegler, graduate thesis, University Bayreuth, Herbert Utz-Verlag, Munich, p. 34, **2001**

[8]   data base WIAM metallinfo at KIT, for information see under http://www.wiam.de/home.php, last access 11.06.2013

[9]   Email communication from 12.11.2012 with Mr. M. Oehler, TRUMPF

[10]   H. Hügel, T. Graf *Laser in der Fertigung*, Vieweg & Teubner, 2nd Ed. Wiesbaden, ISBN 978-3-8351-0005-3, p. 3, **2009**

[11]   Binary Al-Si Phase diagram, see online library for Al-Si under http://www.springermaterials.com/docs/pdf/10655491_51.html , last access: 17.06.2013

[12]   J. Schmid, G. Barbezat, *Metallische Verbundwerkstoffe für die Zylinderlaufbahnen von Verbrennungsmotoren und deren Endbearbeitung durch Honen*, Chapter 9 in *Metallische Verbundwerkstoffe*, by K. U. Kainer (Ed.), pp. 232, Wiley-VCH Weinheim, ISBN 3-527-30532-7, **2003**

[13]   V. Uhlenwinkel, L. Achelis, K. Bauckhage (Ed.`s), *Symposium Sprühkompaktieren*, vol. 7, Universität Bremen, SFB 372, **2004**